



HAL
open science

Modeling longitudinal dispersion in variable porosity porous media : control of velocity distribution and microstructures

Philippe Gouze, Alexandre Puyguraud, Thierry Porcher, Marco Dentz

► To cite this version:

Philippe Gouze, Alexandre Puyguraud, Thierry Porcher, Marco Dentz. Modeling longitudinal dispersion in variable porosity porous media : control of velocity distribution and microstructures. *Frontiers in Water*, 2021, 10.3389/frwa.2021.766338 . hal-03396794v2

HAL Id: hal-03396794

<https://hal.umontpellier.fr/hal-03396794v2>

Submitted on 25 Oct 2021

HAL is a multi-disciplinary open access archive for the deposit and dissemination of scientific research documents, whether they are published or not. The documents may come from teaching and research institutions in France or abroad, or from public or private research centers.

L'archive ouverte pluridisciplinaire **HAL**, est destinée au dépôt et à la diffusion de documents scientifiques de niveau recherche, publiés ou non, émanant des établissements d'enseignement et de recherche français ou étrangers, des laboratoires publics ou privés.

Modeling longitudinal dispersion in variable porosity porous media : control of velocity distribution and microstructures.

Philippe Gouze^{1,*}, Alexandre Puyguiraud², Thierry Porcher¹ and Marco Dentz²

¹*Geoscience Montpellier, CNRS, Université de Montpellier, Montpellier, France*

²*Spanish National Research Council (IDAEA-CSIC), Barcelona, Spain*

Correspondence*:

Philippe.Gouze@umontpellier.fr

2 ABSTRACT

3 Hydrodynamic dispersion process in relation with the geometrical properties of the porous media
4 are studied in two sets of 6 porous media samples of porosity θ ranging from 0.1 to 0.25. These
5 two sets of samples display distinctly different evolutions of the microstructures with porosity but
6 share the same permeability trend with porosity. The methodology combines three approaches.
7 First, numerical experiments are performed to measure pre-asymptotic to asymptotic dispersion
8 from diffusion-controlled to advection-controlled regime using Time-Domain Random Walk solute
9 transport simulations. Second, a porosity-equivalent network of bonds is extracted in order to
10 measure the geometrical properties of the samples. Third, the results of the direct numerical
11 simulations are interpreted as a Continuous Time Random Walk (CTRW) process controlled by
12 the flow speed distribution and correlation. These complementary modelling approaches allow
13 evaluating the relation between the parameters of the conceptual transport process embedded in
14 the CTRW model, the flow field properties and the pore-scale geometrical properties. The results
15 of the direct numerical simulations for all the 12 samples show the same scaling properties of the
16 mean flow distribution, the first passage time distribution and the asymptotic dispersion versus the
17 Péclet number than those predicted by the CTRW model proposed by Puyguiraud et al. (2021). It
18 allows predicting the asymptotic dispersion coefficient D^* from $Pe = 1$ to the largest values of
19 Pe expected for laminar flow in natural environments ($Pe \approx 4000$). $D^* \propto Pe^{2-\alpha}$ for $Pe \geq Pe^{crit}$,
20 where α can be inferred from the Eulerian flow distribution and Pe^{crit} depends on porosity. The
21 Eulerian flow distribution is controlled by the distribution of fractions of fluid flowing at each of the
22 pore network nodes and thus is determined mainly by the distribution of the throat radius and the
23 coordination number. The later scales with the number of throats per unit volume independently
24 on the porosity. The asymptotic dispersion coefficient D^* decreases when porosity increases for
25 all Péclet values larger than 1 due to the increase with porosity of both α and the flow speed
26 decorrelation length.

1 INTRODUCTION

27 Modeling transport of solute in porous media is a prerequisite for many environmental and engineering
28 applications, ranging from aquifers contaminant risk assessment to industrial reactors, filters and batteries
29 design. The solutes can be pollutants, reactants and products involved in solute-solute or solute-mineral
30 reactions, but also (bio-)nanoparticles or nutrients involved in the growth of bio-mass. The mechanism
31 under consideration is the spatial dispersion which leads to the spreading and the mixing of dissolved

32 chemicals, thus controlling the potential reactions in the flowing fluid and between the fluid and the porous
 33 media (Bear, 1972; Brenner and Edwards, 1993; Dentz et al., 2011). The dispersion process has been,
 34 and still is, a largely studied topic in the field of geosciences because rocks at depth are, as a general
 35 rule, porous media saturated with fluid(s) that move due to natural or artificial pressure gradients, and
 36 display a large spectrum of heterogeneities. In all these domains, reliable predictive models that can be
 37 parameterized by direct measurements are necessary, for example, to monitor and assess risks linked to
 38 the use of underground water resources, or in the course of industrial operations, such as hydrocarbon
 39 exploitation and CO₂ or underground nuclear waste storage.

40 Hydrodynamic dispersion is the macroscopic result of the mass transfers by diffusion and advection
 41 that occurs at the pore scale (Whitaker, 1967; Sahimi, 2011; De Anna et al., 2013). Together, diffusion
 42 and advection of solute produce a large spectrum of dispersion features because (natural) porous media
 43 display complex structures inducing a large diversity of velocity fields, and thus distinctly different speed
 44 distributions and spatial correlations. Probably the most obvious behavior that illustrates the complexity
 45 of dispersion mechanisms in porous media is the variably-lasting pre-asymptotic dispersion regime that
 46 cannot be modeled by a single Fickian dispersion coefficient. Pre-asymptotic, or non-Fickian, dispersion
 47 is commonly observed in laboratory experiments (Moroni and Cushman, 2001; Levy and Berkowitz,
 48 2003; Seymour et al., 2004; Morales et al., 2017; Carrel et al., 2018; Souzy et al., 2020), and numerical
 49 simulations (Bijeljic et al., 2011, 2013; De Anna et al., 2013; Icardi et al., 2014; Kang et al., 2014; Li
 50 et al., 2018; Puyguiraud et al., 2019c). It is characterized by heavy-tailed arrival time distributions $f_t(t)$
 51 and super-diffusive growth of the longitudinal displacement variance $\sigma^2(t)$. For a given porous medium,
 52 the duration of the non-Fickian regime is controlled by solute particles that move the slowest, which
 53 emphasizes the determinant role of both the regions where the velocity is low and the tortuosity of the
 54 flow paths. Asymptotically, dispersion converges toward Fickian behavior, characterized by the constant
 55 longitudinal dispersion coefficient D^* (Bear, 1972; Brenner and Edwards, 1993).

56 Evaluating the longitudinal asymptotic dispersion coefficient D^* is a fundamental issue, because most
 57 operational modeling tools have been constructed around the Fickian advection-dispersion equation that
 58 reads for transport in the direction of the mean flow, here the z -direction, (Bear, 1972):

$$59 \quad \frac{\partial \theta c(z, t)}{\partial t} - \frac{\partial}{\partial z} \left[\theta D^* \frac{\partial c(z, t)}{\partial z} + u_z(z) c(z, t) \right] = 0, \quad (1)$$

61 where c is the solute concentration, θ is the connected porosity, $u_z = \theta \langle v_z \rangle$ denotes Darcy's velocity, with
 62 $\langle v_z \rangle$ being the mean pore velocity.

63 Many experimental studies and mathematical developments on dispersion using mainly simple porous
 64 media have been performed since the pioneering works of Danckwerts (1953). The reader will find an
 65 exhaustive review of the different results and models of both longitudinal and transverse dispersion in
 66 Delgado (2006). A main well-observed feature of longitudinal dispersion D^* is its non-linear increase
 67 with the mean flow velocity. It is recognized since the pioneering works of Saffman (1959) and then Bear
 68 (1972). It is generally expressed in terms of D^*/d_m versus the Péclet number $Pe = \langle v_e \rangle \ell / d_m$, where ℓ is a
 69 characteristic length, d_m is the molecular diffusion coefficient and $\langle v_e \rangle$ is the mean Eulerian flow speed
 70 ($v_e = \sqrt{v_x^2 + v_y^2 + v_z^2}$, with v_i denoting the flow velocity component i , see Section 2.2). Simulations in
 71 networks of constant velocity tubes (Sahimi and Imdakm, 1988) of radius r following distributions such as

72 $P(r) \propto re^{-r^2}$ (Chatzis and Dullien, 1985) indicated a relation of the form

73
$$D^*/d_m \propto Pe^\beta, \quad (2)$$

75 with $\beta = 1.2 \mp 0.1$ (Sahimi, 2011), while for instance $\beta = 2$ in a single tube (Taylor, 1953). For infinite
 76 Pe , experimental particle tracking results (e.g. Souzy et al., 2020) give the relation $D^*/d_m \approx Pe$, where
 77 the characteristic length ℓ is of the order of the pore length. However, it is worth noticing that in Souzy
 78 et al. (2020)'s experiments the lowest velocities cannot be measured because they use finite-size particles
 79 that cannot access to the vicinity of the solid. Interestingly, the behavior (2) with $\beta \simeq 1.2$ was cited in
 80 numerous studies concerning bead-packs and homogeneous sand-packs for intermediate Péclet numbers
 81 (Pfannkuch, 1963; Han et al., 1985; Seymour and Callaghan, 1997; Sahimi et al., 1986; Bijeljic et al., 2004).
 82 For instance, particle tracking simulations in pore-networks reported in Bijeljic and Blunt (2006) gave
 83 $\beta = 1.2$, for $Pe < 400$ and $\beta = 1$, for $Pe > 400$. Conversely, similar numerical simulations (using random
 84 walk particle tracking) performed by Puyguiraud et al. (2021) using digitized images of consolidated
 85 sandstone, gave a value of $\beta = 1.65$ for $10 \leq Pe \leq 10^5$. The few experimental data on rocks (obviously
 86 more heterogeneous than bead-packs) displayed a broader range of behaviors; for example Kinzel and Hill
 87 (1989) reported $1.30 \leq \beta \leq 1.33$. However, it is worth noticing that evaluating dispersion in rocks, for a
 88 large range of Pe values, either at laboratory or field scale from tracer tests is challenging. For instance,
 89 controlling the boundary conditions and verifying that the tracer is conservative are some of the known
 90 issues that may introduce errors in the estimation. Yet, the main issue is probably linked to the fact that, by
 91 definition, the experimental results are interpreted using the Fickian model, whereas it is difficult to prove
 92 that dispersion is asymptotic without being able to measure the tracer breakthrough curves over several
 93 orders of magnitude in order to capture the low speed fraction of the solute transport (Gouze et al., 2008).
 94 We will show in Section 3.4 that measuring asymptotic dispersion for large values of Pe in natural porous
 95 media is in fact virtually impossible using cm- or even meter-scale experiments.

96 While measuring dispersion experimentally is burdensome, modeling approaches are now mature to
 97 perform numerical experiments. Direct numerical simulations (DNS) are unique tools for investigating
 98 both the pre-asymptotic and the asymptotic behavior in a common frame. They can be used to accurately
 99 measure D^* , but also to study the mechanisms that produce dispersion in relation with the measurable
 100 (average) properties of the material, and to test upscaling theories. Recent works (Bijeljic and Blunt,
 101 2006, 2007; De Anna et al., 2013; Puyguiraud et al., 2019a, 2021) showed that hydrodynamic transport in
 102 porous media can be adequately conceptualized and modeled by a continuous time random walk (CTRW)
 103 that models streamwise transport through particle transitions over fixed spatial distance with a transition
 104 time given by the local flow speed and diffusion. The spatial distance at which particles speed changes
 105 corresponds to the decorrelation distance ℓ_c of the mean flow speed. The CTRW integrates in a statistical
 106 framework parameters that are similar to the classical representation of porous media as a network of
 107 throats and pores. As such one can be tempted to investigate how ℓ_c , which is a major ingredient of the
 108 CTRW model, is related to the topological and geometrical properties of the real 3-dimensional pore
 109 network. Moreover, the CTRW model predicts that asymptotic dispersion is controlled by the dispersion
 110 evolution during the pre-asymptotic regime which itself is controlled by the flow speed distribution. How
 111 the later is related to the properties of the pore network is a further issue that requires investigation.

112 The main objective of the present study, is to investigate the relation between the longitudinal dispersion
 113 D^* (and its evolution with the mean flow rate) and the porous media microstructural properties in the frame
 114 of the theory proposed by Puyguiraud et al. (2021) which gives a generalized explanation of longitudinal

115 dispersion (from pre-asymptotic to asymptotic regimes) and a formal relation between dispersion and the
 116 properties of the flow field (velocity distribution, velocity spatial decorrelation and flow path tortuosity).

117 The core of this study is a set of about 150 numerical experiments designed to measure pre-asymptotic
 118 to asymptotic dispersion from diffusion-controlled to advection-controlled regime in 12 sandstone-like
 119 samples of porosity ranging from 10 to 25%. For that, one first computes the steady-state Stokes flow field
 120 from which, the flow speed distribution and the decorrelation distance as well as advective tortuosity are
 121 derived. Then, the direct numerical simulation (DNS) of solute transport at pore scale, involving diffusion
 122 and advection, are performed using Time-Domain Random Walk (TDRW). The dispersion mechanisms are
 123 characterized from the time-resolved particles displacement variance and the first passage time distribution
 124 (FPT) given as outputs of the TDRW simulations. In parallel, the geometrical properties of the porous
 125 samples are evaluated from the computation of the bonds network model (BNM) for each of the samples,
 126 that is obtained from the medial axis transform, or skeletonization, of the connected porosity. This gives
 127 us the unique opportunity to characterize the topology of the connected porosity including the number of
 128 throats (bonds) and pores (network nodes) and the coordination (number of throats per pore), as well as
 129 the throat radius and length. Then, the results of the direct numerical simulations are analyzed in the light
 130 of the CTRW theory proposed by Puyguiraud et al. (2021) which provides quantitative links between the
 131 tail behaviors of the FPT distribution $f_t(t)$, the distribution of flow speeds v_e , the particles displacement
 132 variance $\sigma^2(t)$ and the asymptotic dispersion coefficient D^* scaling with the Pe value.

133 The methodology, including the conceptual and numerical tools used in this study are detailed in Section 2.
 134 The geometrical and topological characteristics of the samples and the flow field properties are presented
 135 in Section 3. The results of the direct numerical simulation of solute transport and the calculation of the
 136 dispersion coefficient for a large range of values of Pe are discussed in Section 3.4. The conclusions of this
 137 study are exposed in Subsection 4.

2 METHODOLOGY

138 2.1 Porous media samples

139 The porous media are binary images made of 480^3 regular voxels (cubes) that are either void or solid.
 140 The first set of 6 samples, noted $FSxx$, where xx is replaced by the porosity value expressed in percent (ex:
 141 $FS13$ for the sample with $\theta=0.13$) was downloaded from the Digital Rocks Portal (Berg, 2016a). They
 142 were generated with the commercial software e-Core following a methodology described in (Oren, 2002)
 143 in order to mimic Fontainebleau sandstone at different porosity (Berg, 2016b). The op. cit. author indicated
 144 that they use identically parameterized silica grain sedimentation and compaction processes typical for
 145 Fontainebleau sandstones, the different porosity values (0.10, 0.13, 0.15, 0.21 and 0.25) being obtained by
 146 varying the amount of silica cement. As such, this process mimics the progressive diagenetic cementation
 147 by silica precipitation (from $FS25$ to $FS10$) of an initially poorly cemented sandstone. Conversely, we
 148 made the second set of samples by step-by-step homogeneous erosion of the solid phase starting from
 149 $FS10$. By removing 1 to 6 layers of solid at the solid-void interface we obtain 6 samples, denoted $FSDxx$
 150 of porosity 0.12, 0.15, 0.17, 0.20, 0.23 and 0.25. This process mimics homogeneous dissolution of the
 151 silica material. The top panel in Figure 1 displays the three-dimensional structure of the lowest porosity
 152 sample $FS10$, and the highest porosity samples $FS25$ and $FSD25$. It can be qualitatively appraised that
 153 the cement precipitation model used to construct $FS25$ increases the number of pores compared $FS10$,
 154 while the pore size is kept roughly similar. In contrast, the dissolution process producing $FS25$ from $FS10$
 155 acts as increasing strongly the pore size, while the number of pores remains roughly unchanged. This set of
 156 sample is viewed as ideal for investigating dispersion of end-members of natural sandstones.

157 **2.2 Flow**

158 Flow simulations are performed on the three-dimensional binary images. The mesh used for solving the
 159 flow is obtained by dividing each of the image voxels by 2 in each of the directions so that 1 voxel of the
 160 raw image is represented by 8 cubic cells of size $\Delta x = \Delta y = \Delta z = 2.85 \times 10^{-6}$ m. This procedure is
 161 applied for improving the resolution of the flow field in the smallest throats (Gjetvaj et al., 2015). The
 162 resulting discretization for the regular grid consists of 960^3 cubic cells. We are considering steady-state
 163 flow of an non-compressible Newtonian fluid at low Reynolds number so that the pore-scale flow velocity
 164 $\mathbf{v}(\mathbf{x})$ is given by the Stokes equation

165
$$\mu \nabla^2 \mathbf{v}(\mathbf{x}) - \nabla p(\mathbf{x}) = 0, \quad (3)$$

167 where $p(\mathbf{x})$ is the fluid pressure. Stokes flow is solved using the finite volume SIMPLE (SemiImplicit
 168 Method for Pressure Linked Equations algorithm) scheme implemented in the SIMPLEFOAM solver of
 169 the OpenFOAM platform (Weller et al., 1998). Twenty layers are added at the inlet and outlet in order to
 170 minimize boundary effects (Guibert et al., 2016). The main flow direction is considered in the z -direction
 171 all over this study. We prescribe 1) a macroscopic pressure gradient $\nabla^* p$ between the inlet ($z = 0$) and
 172 the outlet ($z = Lz$) boundary conditions such that the Reynolds number Re is smaller than 10^{-6} , i.e.
 173 laminar flow and 2) no-slip conditions at the void-solid interfaces and at the remaining boundaries of
 174 the sample. After convergence, that is, once the normalized residual of the pressure and of the velocity
 175 components is below 10^{-5} between two consecutive steps, we extract the components of the velocity at
 176 the voxel interfaces (v_x, v_y, v_z). The results of the flow simulations allow us to extract the three properties
 177 that control dispersion according to Puyguiraud et al. (2019b): 1) the Eulerian speed distribution $p_e(v)$ 2)
 178 the decorrelation distance ℓ_c and 3) the advective tortuosity χ_a . These fundamental flow properties are
 179 respectively displayed in Figures 5, 6, and 7, and discussed in Section 3.

180 **2.3 Solute transport**

181 Pore-scale hydrodynamic transport is classically modeled by the advection-diffusion equation

182
$$\frac{\partial c(\mathbf{x}, t)}{\partial t} - \nabla \cdot [d_m \nabla + \mathbf{v}(\mathbf{x})] c(\mathbf{x}, t) = 0, \quad (4)$$

184 where $c(\mathbf{x}, t)$ is the solute concentration at position \mathbf{x} and time t , d_m is the molecular diffusion coefficient
 185 which is set equal to $d_m = 10^{-9}$ m²/s, and $\mathbf{v}(\mathbf{x})$ is the flow velocity at position \mathbf{x} which is obtained by
 186 solving the Stokes problem (see Section 2.2). Here we use the time domain random walk (TDRW) method
 187 that is based on a finite volume discretization of Equation (4) (Delay et al., 2005). A detailed description
 188 of the TDRW method, its derivation and implementation using voxelized binary images can be found
 189 in Dentz (2012) and Russian et al. (2016); the main features of the method are given below. A study of the
 190 performance and accuracy of the TDRW method for a large range of values of the Péclet number can be
 191 found in (Gouze et al., 2021). The domain discretization used for transport is that used for computing the
 192 flow, i.e., 960^3 cubic voxels .

193 The TDRW method is a grid-based method that models the displacement of particles in space and time
 194 according to the master equation that results from a finite volume discretization of the advection-diffusion
 195 equation. The ensemble average of the particle displacement gives the solution of the transport equation.
 196 A particle transition corresponds to a single transition of a constant length $\xi = \Delta x$ from the center of a
 197 voxel j to the center of one of the 6 face-neighboring voxels i . The direction and the transition duration are
 198 random variables ruled by the local values of the fluid velocity at the voxel interface embedded into the

199 local coefficients b_{ij} (Russian et al., 2016)

$$200 \quad b_{ij} = \frac{d_m}{\xi^2} + \frac{|v_{ij}|}{2\xi} \left(\frac{v_{ij}}{|v_{ij}|} + 1 \right), \quad (5)$$

201 where v_{ij} is the velocity component of \mathbf{v}_j in the direction of voxel i , $v_{ij} = \mathbf{v}_j \cdot \boldsymbol{\xi}_{ij}$. Voxel i is downstream
 202 from voxel j if $v_{ij} > 0$, as a convention. The velocity at the solid-void interface is zero and $d_m = 0$ if
 203 voxel i is a solid voxel. The recursive relations that describe the random walk from position \mathbf{x}_j to position
 204 \mathbf{x}_i of a given particle transition n are

$$205 \quad \mathbf{x}_i(n+1) = \mathbf{x}_j(n) + \boldsymbol{\xi}, \quad t(n+1) = t(n) + \tau_j. \quad (6)$$

206 The probability p_{ij} for a transition of length ξ from voxel j to voxel i is

$$207 \quad p_{ij} = \frac{b_{ij}}{\sum_{[jk]} b_{kj}}, \quad (7)$$

208 where $\sum_{[jk]}$ denotes the summation over the nearest neighbors of voxel j . The transition time τ_j is
 209 independent on the transition direction and is exponentially distributed $\psi_{\tau_j}(t) = \bar{\tau}_j \exp(-t/\bar{\tau}_j)$ with $\bar{\tau}_j$
 210 the mean transition time from voxel j ;

$$211 \quad \bar{\tau}_j = \frac{1}{\sum_{[jk]} b_{kj}}. \quad (8)$$

212 The algorithm consists in computing once the probability p_{ij} (7) and the mean transition time $\bar{\tau}_j$ (8) for
 213 each of the voxels belonging to the pore space and then solving the random walk (6) in which the direction
 214 for each particle transition is drawn from the p_{ij} vector and the transition time is drawn from the exponential
 215 distribution of mean $\bar{\tau}_j$.

216 2.3.1 Simulation setup

217 For each sample, we performed simulations for different values of the Péclet number. The Péclet number
 218 is defined as $Pe = \langle v_e \rangle \lambda / d_m$ where λ is the mean throat length that is displayed for the 12 samples in
 219 Figure 2 and ranges from $6.5 \times 10^{-5} \text{m}$ to $8.8 \times 10^{-5} \text{m}$. The different flow fields used for the TDRW
 220 simulations at different Péclet numbers are obtained by multiplying the raw flow field resulting from the
 221 Stokes simulation by a constant.

222 A *pulse* of constant concentration at the sample inlet ($z = 0$) is applied at $t = 0$ by locating particles
 223 in a flux weighted injection mode. Note that the *pulse* is formally an exponential distribution function
 224 of characteristic time $\tau_j|_{z=0}$ whose mean value is negligible compared to the mean time required for the
 225 particles to move through the sample (Russian et al., 2016). Flux weighted injection means that the number
 226 of particles injected at a location is proportional to the local velocity. This corresponds to a constant
 227 concentration Dirichlet boundary condition. Particles that reach the sample outlet with a speed v_{out} are
 228 reinjected randomly at the inlet plane at a position \mathbf{x} satisfying the condition $|\mathbf{v}_x - v_{out}| \ll \langle v \rangle$.

229 The distribution (PDF) of first passage times at a given distance Z from the injection location, that
 230 denotes the solute breakthrough curve (BTC) usually measured in laboratory or field tracer tests, is noted
 231 $f_t(t)$ (Figure 8). The apparent longitudinal dispersion coefficient $D(t)$ is evaluated from the displacement
 232 variance $\sigma_z^2(t)$ of the particles (Fischer, 1966):

$$D(t) = \frac{1}{2} \frac{d\sigma_z^2(t)}{dt}, \quad (9)$$

233 with $\sigma_z^2(t) = \langle (z(t) - \langle z \rangle)^2 \rangle - \langle z(t) - \langle z \rangle \rangle^2$. The asymptotic longitudinal dispersion coefficient $D^* =$
 234 $\sigma_z^2(t)/2t$ is obtained for $t > t^*$, where t^* is the time required for all the particles to sample the entire
 235 heterogeneity, i.e. when $\sigma_z^2(t) \sim t$ (see for example Figure 10).

236 2.4 The equivalent bond network model

237 We compute the bond network model (BNM) for each of the *FS* and *FSD* samples in order to extract
 238 the geometrical and topological characteristics of the connected porosity. The methodology to obtain
 239 the network representation of the connected porosity of the sample includes two main steps. The first
 240 one is the extraction of the void space skeleton which is the one-dimensional continuous object centrally
 241 located (and spatially referenced) inside the pore space. The skeleton can be computed using different
 242 approaches; here we used a thinning algorithm inspired from the works of Lee et al. (1994) that provides
 243 the local medial-axis. The coordinate of the skeleton is known with a spatial resolution equivalent to that of
 244 the original 3D-image and associated with the local hydraulic radius r_l normal to the local medial axis
 245 that is evaluated using a pondered 45 degree multi-ray method. Thus, the skeleton keeps the relevant
 246 geometrical and topological features of the pore space (Siddiqi and Pizer, 2008). The second step consists in
 247 transforming the skeleton into a network of bonds and nodes that connect three or more bonds. This yields
 248 an irregular lattice. The length λ of a given bond is the sum of the length of the skeleton components used
 249 to built this bond, so that the local tortuosity of the skeleton is embedded into λ . For each bond, the radius
 250 r_h is obtained from the harmonic means (noted $\langle \rangle_H$) of the local conductance, so that $r_h = (\langle r_l \rangle_H)^{1/4}$. The
 251 algorithm is non-parametric; there is no assumption on any of the characteristics of the obtained lattice.

252 2.5 Upscaled CTRW model

253 Puyguiraud et al. (2021) proposed a continuous time random walk (CTRW) model that describes transport
 254 through particle transitions over the length ℓ_c with a transition time that is given by the local flow speed
 255 and diffusion. The central assumption of this model is that transition times at subsequent CTRW steps are
 256 independent identically distributed random variables. Furthermore, it is assumed that particles move at the
 257 mean pore velocity, that is, it is assumed that during a transition particles are able to diffusively sample the
 258 velocities across pore conducts. The scale ℓ_c is set equal to the decorrelation distance of particle speeds so
 259 that subsequent particle speeds can be considered statistically independent. The distribution of the Eulerian
 260 mean flow speeds $p_m(v)$ is obtained from the Eulerian speed PDF as

$$p_m(v) = -2v \frac{dp_e(2v)}{dv}. \quad (10)$$

261 As particles move at equidistant spatial steps, they sample flow speeds in a flux-weighted manner. This
 262 is due to the fact that particles are distributed at pore intersections according to the relative downstream
 263 fluxes. Thus, the distribution $p_v(v)$ of subsequent particle speeds are related to the distribution of Eulerian
 264 mean flow speeds through flux-weighting as (Puyguiraud et al., 2021)

$$p_v(v) = \frac{v p_m(v)}{\langle v_m \rangle}. \quad (11)$$

At each turning point of the CTRW, particles are assigned a random speed from $p_v(v)$. The particle transition time distribution $\psi(t)$ reflects both advection and diffusion. It is cut-off at times larger than $\tau_D = \ell_c^2/d_m$, the diffusion time over the decorrelation distance. For times small compared to the cut-off time, $\psi(t)$ can be approximated by

$$\psi(t) = \frac{\ell_c^2}{t^3 \langle v_m \rangle} p_m(\ell_c/t). \quad (12)$$

265 At times larger than τ_D it is cut-off exponentially fast.

266 The flow speed distribution is at the center of the transport process. In porous media, such as rocks, the
 267 mean flow speed can often be approximated by a Gamma-type distribution (Dentz et al., 2018; Puyguiraud
 268 et al., 2019b; Souzy et al., 2020) and displays a power-law scaling $p_e(v) \sim v^{\alpha-1}$ for $v < \langle v_m \rangle$. For sphere
 269 packs and simple structures such as sand-pack the linear flow profile close to the grains (due to the no-slip
 270 boundary condition) implies that $p_e(v)$ is flat at low velocities, so that $\alpha \simeq 1$ (Dentz et al., 2018). In more
 271 heterogeneous porous media, other values of α are expected. For example, Puyguiraud et al. (2021) found
 272 $\alpha \approx 0.35$ for a Berea sandstone sample. For such Gamma-type distributions, $p_e(v) \sim v^{\alpha-1}$ at small flow
 273 speeds, $\psi(t)$ behaves for high Péclet numbers as $\psi(t) \sim t^{-2-\alpha}$ before the exponential cut-off at times
 274 larger than τ_D . The tortuosity of particle trajectories in this framework is given by the ratio of the mean
 275 asymptotic particle speed $\ell_c/\langle \tau \rangle \equiv \langle v_e \rangle$ (where $\langle \tau \rangle$ denotes the particle mean travel time) and the mean
 276 streamwise flow velocity $\langle v_z \rangle$. Furthermore, for this type of flow speed distributions, the CTRW approach
 277 predicts some further interesting scaling laws that can be verified from direct numerical simulations. The
 278 behavior of particle breakthrough curves $f(t, Z)$ at a control plane located at the streamwise location Z is
 279 analogous to the behavior of $\psi(t)$. They show a power-law dependence as $f(t, Z) \sim t^{-2-\alpha}$ if $Z/v_z \ll \tau_D$
 280 (i.e., the peak time is much smaller than the cut-off time), and exponential decay for times larger than the
 281 cut-off time τ_D . The predicted dependence of the asymptotic longitudinal dispersion coefficients on the
 282 Péclet number is for $Pe \gg 1$

$$\frac{D^*}{d_m} \sim Pe^{2-\alpha} \quad (13)$$

for $0 < \alpha < 1$ and

$$\frac{D^*}{d_m} \sim Pe \ln Pe \quad (14)$$

283 for $\alpha = 1$, see also Saffman (1959) and Koch and Brady (1985).

284 To sum-up, this upscaled model, constructed on the representation of the hydrodynamic transport as a
 285 CTRW process in a 1-dimensional network of bonds, is fully constrained, for any values of $Pe > 1$ by the
 286 knowledge of the distribution of Eulerian flow speeds $p_e(v)$ and the decorrelation distance ℓ_c of particle
 287 speeds.

288 From here one can recognize on one hand the complementarity of the BNM and the DNS to explore the
 289 relation between the dispersion and the pore network characteristics, and on the other hand the conceptual
 290 framework that links the CTRW model and the BNM representation of the porous medium. This emphasizes
 291 the possibility of 1) relating the distribution of the Eulerian flow speed to the large scale transport behavior
 292 and 2) characterizing dispersion for different porous media based on the knowledge of the flow speed
 293 distribution. Indeed, the BNM gives us the information on the real topology of the pore network as
 294 well as the distribution and the average of bond properties (radius and length), while the DNS provides
 295 the information on the flow field (speed distribution and decorrelation distance as well as the advective
 296 tortuosity).

3 PORE NETWORK PROPERTIES, FLOW FIELDS AND DISPERSION

297 The top row in Figure 1 illustrates the 3-dimensional structure of sample *FS10* ($\theta = 0.1$) and of both *FS25*
 298 and *FSD25* sharing the same porosity $\theta = 0.25$. The bottom row in Figure 1 displays flow lines (and the
 299 local velocity) within the connected porosity for these three samples and gives a qualitative appraisal of the
 300 dissimilarities between the lowest porosity and the highest porosity samples on one hand, and on the other
 301 hand those occurring between the highest porosity sample of each of the two sets in relation with the pore
 302 network structures. In the following we will quantify these differences and their implications on dispersion.

3.1 Connected porosity geometrical properties retrieved from the BNM

303 As explained in Section 2.1, we computed the Bond Network Model (BNM) for each of the 12 samples,
 304 in order to evaluate the topology and the geometry of the connected porosity and specifically how these
 305 characteristics change with the sample porosity for the *FS* and the *FSD* sets of samples. The main
 306 properties versus porosity are summarized in Figures 2 and 3. The topology of the connected porosity is
 307 characterized by the number of throats (network bonds) and pores (network nodes) per volume of rock
 308 (here the reference is the sample volume) as well as the coordination number κ that denotes the mean
 309 number of throats connected to a given pore. The bonds are characterized by the mean of the radius r_h and
 310 length λ and by the radius r_h distribution displayed in Figure 4.

312 For the *FS* set, decreasing porosity from the highest to the lowest porosity values is obtained by allocating
 313 increasing amounts of cement into localized clusters that acts as increasingly closing connections and thus
 314 decreasing the number of pores and throats and the coordination number. The fixed distribution of the
 315 cement clusters determines the length of the bonds independently of the porosity ($\lambda \approx 65\mu m$), but volume
 316 conservation imposes that the hydraulic radius r_h increases with porosity. The distribution of $r_h/\langle r_h \rangle$ is
 317 wide, decreases almost monotonically from small to high r_h and does not depend on porosity.

318 For the *FSD* set, increasing porosity from the lowest to the highest is obtained by homogeneous erosion
 319 of the solid phase, i.e. both the grains and the cement. The number of pores and throats as well as κ first
 320 decreases for $\theta \leq 0.15$ caused by merging of adjacent throats following a process which is roughly the
 321 opposite of that described for the *FS* set of samples. Then, the number of pores and throats stays almost
 322 constant for $\theta > 0.15$. As a result, the increase of porosity is mainly due to the increase of the throat length
 323 λ and radius r_h . The distribution of $r_h/\langle r_h \rangle$ is almost Gaussian around the mean value, and independent of
 324 the porosity for $\theta > 0.15$. The transition from the original sample *FS10* to the *FSD12* and then *FSD15*
 325 is well visible in the r_h distribution. Note that, as soon as the throats are widely distributed like for the *FS*
 326 set of samples, κ is an indicator of the potential local flow rate disorder at the network nodes because the
 327 probability of having upstream and downstream bonds of distinctly different flow rates is high.

328 Altogether, these results show that the two sets of samples are very different in terms of 1) the topology
 329 of the network; for the *FSD* set, the topology is almost similar for all the porosity range, while it is

330 increasingly complex (with increasing tortuosity, see discussion below) as porosity decreases for the *FS*
 331 set of samples, and 2) the characteristic size of the throats that is almost independent of the porosity for the
 332 *FD* set whereas it increases with porosity for the *FSD* set.

333 3.2 Permeability and flow field properties

334 Permeability values k for the 12 samples computed using Darcy's law ($k = \bar{v}_z \mu / \nabla^* p$) are plotted in
 335 the left panel of Figure 5. Permeability increases from $1.4 \times 10^{-13} \text{m}^2$ for sample *SF10* to $6.04 \times 10^{-12} \text{m}^2$
 336 ($6.08 \times 10^{-12} \text{m}^2$) for sample *SF25* (*SFD25*) and are all aligned with the relation $k \sim \theta^4$ independently on
 337 geometrical characteristics of the pore space. The permeability computed on the BNM (solving a Kirchhoff
 338 problem) is also reported Figure 5 in order to evaluate the accuracy of the BNM.

339 The right panel of Figure 5 displays the advective tortuosity χ_a , i.e. the mean tortuosity of the flow
 340 lines. The advective tortuosity is obtained from the ratio of the mean Eulerian speed v_e to the mean
 341 velocity in the direction of the flow v_z (Koponen et al., 1996; Ghanbarian et al., 2014; Puyguiraud et al.,
 342 2019c): $\chi_a = \langle v_e \rangle / \langle v_z \rangle$. For both the set of samples, χ_a decreases when porosity increases, but it is more
 343 pronounced for the *FS* set of samples. These trends seem to be mainly controlled by the increase of the
 344 throat radius as porosity increases, while the topological characteristic of the network plays a minor role
 345 which is probably resulting from a complex coupling of the geometrical and topologically parameters
 346 discussed above. This makes the advective tortuosity, which is one of the three parameters of the CTRW
 347 model proposed by Puyguiraud et al. (2021), an intrinsic characteristic of the hydrodynamic system that is
 348 essentially porosity-dependant.

349 The distributions of the Eulerian mean speed for the 12 samples are plotted in Figure 6. The dissimilarity
 350 of the $p_m(v)$ curves between the *FS* and the *FSD* sets is clearly visible. The *FSD* samples are displaying
 351 almost the same mean speed distributions with power-law trend $p_m(v) \sim v^{\alpha-1}$ for $v < \langle v_m \rangle$ with
 352 $\alpha = 0.245 \pm 0.05$. For the *FS* set, the evolution of $p_m(v)$ with porosity includes two features. First, $p_m(v)$
 353 gradually diverges from a Gamma distribution as porosity increases, with the occurrence of increasingly
 354 marked transition between the values of speed larger than the mean ($v > \langle v_m \rangle$) and the power-law slope
 355 for the slower speed values. Second, the power-law slope for $v \ll \langle v_m \rangle$ increases when porosity decreases,
 356 ranging from $\beta = \alpha - 1 = 1.63$ for $\theta = 0.25$ to $\beta = 1.75$ for $\theta = 0.10$. These values are in agreement
 357 with the value of 1.65 found by Puyguiraud et al. (2021) for the Beara sandstone. As far as we know,
 358 they have been very few studies of the correlation between the flow speed distribution and the properties of
 359 the pore space microstructures (Siena et al., 2014; Matyka et al., 2016; Alim et al., 2017). For instance,
 360 Alim et al. (2017) investigated this issue using numerical simulations in 2-dimensional simple artificial
 361 porous media made of circular or elliptical discs placed on a square or triangular lattices with increasing
 362 disorder. By extracting and analyzing the corresponding network of tubes, following a procedure quite
 363 similar to that implemented for extracting the BNM (Section 2.4), they concluded that the flow distribution
 364 is mainly determined by the distribution of fractions of fluid flowing at each of the network node and not by
 365 the overall tube size distribution. Our results lead us to a similar conclusion for the complex 3-dimensional
 366 porous media studied here. The evolution of the mean flow speed with porosity for the *FS* set in comparison
 367 with the weak evolution of the mean flow speed with porosity for the *FSD* set appears to be correlated to
 368 the noticeable increase with porosity of the number of throats as well as the mean number of throats per
 369 pore κ (Figure 3) measured for the *FS* set, whereas both the number of throats and κ are almost constant
 370 for the *FSD* set of samples.

371 3.3 Speed decorrelation distance length

372 The decorrelation distance ℓ_c is evaluated from the Lagrangian flux weighted speed autocorrelation
 373 function $\Upsilon_{vv}(l) = \langle (v_v(s) - \langle v_v \rangle)(v_v(s+l) - \langle v_v \rangle) \rangle / \sigma_{v_v}^2$, where l denotes the lag. The decorrelation

374 distance ℓ_c is given by the value of the lag corresponding to $\Upsilon_{vv}(l) = 1/e$. The two panels at left of
 375 Figure 7 display the Lagrangian flux weighted speed autocorrelation function $\Upsilon_{vv}(l)$ for the two set of
 376 samples. The corresponding values of the decorrelation distance ℓ_c versus porosity are given in the third
 377 panel of Figure 7, and the ratio of the decorrelation distance to the mean throat length $\eta = \ell_c/\lambda$ versus
 378 porosity is given in the right panel.

379 For both the sample sets, the decorrelation distance ℓ_c increases with porosity from about $150 \mu\text{m}$ at
 380 $\theta = 0.1$ to about $240 \mu\text{m}$ for *FS* and $290 \mu\text{m}$ for *FSD*. The slight increase of ℓ_c for the *FSD* set for
 381 $\theta > 0.15$ compared to the *FS* set is caused by the increase of the throat radius and the decrease of tortuosity
 382 with porosity that are more important for *FSD* than for *FS*. The ratio η also displays an increase with
 383 porosity following a similar trend for both the *FS* and the *FSD* set of samples, the values for *FSD* being
 384 smaller of ~ 0.5 unit than for *FS*. Thus, in average, the number of bond lengths travelled before losing the
 385 memory of the initial speed ranges from about 2 to 4. These values are in good agreement with the value of
 386 4 obtained by Puyguiraud et al. (2021) by fitting DNS and CTRW for Berea sandstone of porosity 0.18.

387 3.4 Dispersion

388 In this section we are presenting the results of the transport DNS, discussing them in the frame of
 389 the scaling properties derived from the CTRW model proposed by Puyguiraud et al. (2021) and of the
 390 properties retrieved from the BNM (Section 3.1).

391 The first passage time distributions $f_t(t)$ (or breakthrough curves) at a distance of 20 times the sample
 392 size are given in Figure 8 for $Pe = 100$ and also for purely advective transport ($d_m = 0; Pe = \infty$).
 393 For the latter, all the curves display the power-law tailing that characterize pre-asymptotic (non-Fickian)
 394 regime over 3 to 4 orders of magnitude. The scaling $f_t(t) \sim t^{-2-\alpha}$ predicted by Puyguiraud et al. (2021)
 395 with the values of α corresponding to those measured on the mean speed distribution is confirmed for
 396 all the samples. The comparison of the value of α ($0.24 \leq \alpha \leq 0.37$) for the *FS* set of samples is given
 397 in Figure 9. For $Pe = 100$, even if it can be considered a quite large value for natural porous media,
 398 diffusion acts as increasing the rate at which $f_t(t)$ decreases with time and the α -dependent power-law
 399 trend is not present. Note that the beginning of the exponential decrease is visible for *FSD25* at $t \approx 5\tau_D$,
 400 where $\tau_D = \ell_c^2/d_m \approx 80\text{s}$.

401 We now focus on determining the asymptotic dispersion coefficient D^* from the asymptotic regime of
 402 the displacement variance. Figure 10 displays, as an example, the displacement variance normalized to
 403 the throat length (σ^2/λ^2) for the 12 samples in the case $Pe = 100$, but the following comments apply for
 404 all values of Pe larger than 1. All curves converge to the asymptotic regime ($\sigma^2/\lambda^2 \sim t$) for time $t \geq t_a$,
 405 where t_a is independent of the value of Pe but depends on porosity; $t_a \approx 10^3\text{s}$ for $\theta = 0.1$ and $t_a \approx 10^4\text{s}$
 406 for $\theta = 0.25$, i.e. about 40 and 120 times τ_D , respectively. This point is important regarding the possibilities
 407 of measuring the asymptotic dispersion from laboratory experiments, deriving D^* from the breakthrough
 408 curves, for instance. For $Pe = 100$, that corresponds to a mean flow speed of $1.5 \times 10^{-3} \text{ m/s}$ for *FS10*, a
 409 sample of about 1.5 m long displaying the same properties of the mm-scale sample would be necessary
 410 to measure D^* ; a distance of 60 m would be necessary for $Pe = 4000$. This indicates that experimental
 411 measurement of D^* can be performed only for low values of Pe , typically of the order $Pe \leq 10$. However,
 412 for such low values of Pe it is not possible to measure α and thus determine the trend $D^*(Pe)$.

413 Conversely, the DNS allows us to perform numerical experiments over large range of Pe values; Figure 11
 414 displays the value of D^* versus Pe for the 12 samples from diffusion-dominant regime ($Pe = 10^{-3}$)
 415 to advection-dominant ($Pe = 2 \times 10^4$). These curves can be commented in terms of their slope and of
 416 their scaling with porosity, for $Pe \gg 1$. Note that for $Pe \rightarrow 0$ the ratio D^*/d_m is equal to the inverse

417 of the diffusive tortuosity ($D^*/d_m = \chi_d^{-1}$). For both the *FS* and *FSD* sets of samples, the relation
 418 $D^*/d_m \propto Pe^{2-\alpha}$ predicted by the CTRW model for $Pe \gg 1$ is observed. The values of α compared to
 419 those measured using the speed distribution and the tailing of $f_t(t)$ are given in Figure 9. The minimum
 420 value Pe_c at which $D^*/d_m \propto Pe^{2-\alpha}$ is effectively observed, is correlated with the shape of the mean speed
 421 distribution (Figure 6). For *FS10*, the trend $p_m(v) \sim v^{\alpha-1}$ with $\alpha = 0.24$ extends up to $5 \times 10^{-3}v/\langle v_m \rangle$,
 422 while for *FS25* the trend $\alpha = 0.37$ extends up to $3 \times 10^{-4}v/\langle v_m \rangle$ only. This gives values of Pe_c ranging
 423 from 1000 for *FS10* to 50 for *FS25*. The same trend is observed for the *FSD* set of samples. These results
 424 demonstrate the clear control of the particle mean speed distribution on the evolution of D^* with the Péclet
 425 number. However, both the two sets of samples display a scaling of D^* with porosity, independently of
 426 the slope determined for $Pe \geq Pe_c$. The expected decrease of D^* for all values of $Pe > 1$ when porosity
 427 increases, corresponding to a decrease of the slope of $p_m(v)$ for $v \ll \langle v_m \rangle$ is clearly visible for the *FS*
 428 set of samples. But, the results for the *FSD* set, that share the same mean speed distribution (Figure 6),
 429 show also a clear decrease of D^* as porosity increases, which indicates that the dispersion scaling with
 430 porosity is not solely controlled by $p_m(v)$ for $v \ll \langle v_m \rangle$. Indeed, the increase of D^* with porosity is also
 431 related to the increase of the speed decorrelation distance ℓ_c with porosity. In the frame of the CTRW
 432 model ℓ_c denotes the length at which a new velocity is drawn from the mean speed distribution, and as such
 433 ℓ_c determines the rate at which the speed changes.

434 Furthermore, we observe in Figure 11 that D^* shows different power-law behaviors for $Pe < Pe_c$ that
 435 can be related to the scaling behavior of the distribution of mean flow speeds and the transition time
 436 distribution. In the limit of infinite Pe , the transition time distribution is given by (12). For finite Pe , it
 437 is cut-off at the diffusion time τ_D . The log-slope of $\psi(t)$ at the cut-off time depends on the average flow
 438 speed $\langle v_m \rangle$. This is shown in Figure 12, which displays the distribution of purely advective transition
 439 times rescaled by $\tau_v = \ell_c/\langle v_m \rangle$ for *FS10* and *FS25*. The behavior of D^* for $Pe < Pe_c$ corresponds to
 440 the power-law scaling of $\psi(t)$ at dimensionless times equal to Pe . The slope of the $\psi(t)$ curves display
 441 the power-law behaviors $t^{-2-\alpha'}$ for $Pe < Pe_c$ with $\alpha' = 0.38$ and 0.79 for *FS10* and *FS25*, respectively.
 442 For $Pe \geq Pe_c$ the values of α are similar to those reported in Figure 9 for $f_t(t)$, $p_m(v)$ and $D^*(Pe)$, i.e.
 443 $\alpha = 0.23$ and 0.37 for *FS10* and *FS25*, respectively.

4 SUMMARY AND CONCLUSIONS

444 We performed numerical experiments of passive solute transport for two sets of porous media mimicking a
 445 large range of porosity and microstructures expected in sandstones. The aim was to test the validity of the
 446 CTRW model, to explore how the flow field characteristics are linked to the porous media geometrical
 447 properties and to determine the scaling of asymptotic dispersion coefficient D^* with the Péclet number. The
 448 two sets of six samples share similar porosity, ranging from 0.1 to 0.25, and the same permeability-porosity
 449 trend $k(\theta)$ but displays distinctly different microstructures and thus dispersion evolution.

450 The conceptual CTRW model of solute transport in porous media, as the one proposed by Puyguiraud
 451 et al. (2021), infers that solute spreading along particle paths is controlled by the transition time of the
 452 solute particles which is determined by the distribution of solute particle mean speeds $p_m(v)$, the velocity
 453 decorrelation distance ℓ_c and diffusion. The effective tortuosity factor that depends on Pe and on the
 454 advective tortuosity χ_a (that can be also easily evaluated from the flow field) allows mapping dispersion
 455 in the streamwise direction which is aligned with the mean pressure gradient. With decreasing Pe , the
 456 effective tortuosity of the solute particles increases and the control of $p_m(v)$ on dispersion decreases
 457 but remains important up to high values of Pe because of the wide distribution of the particles speeds

458 toward low speed values. This means that for heterogeneous media, such as sandstones, the pre-asymptotic
 459 (non-Fickian) dispersion regime is likely to persist over long time scales.

460 We found that the scaling properties, measured by the coefficient α , predicted by Puyguiraud et al.
 461 (2021)'s model are effectively measurable for all the 12 studied samples. For instance, results shows
 462 that at high Pe , the tail of the breakthrough curves, that is controlled by the low flow speeds, scales as
 463 $f_t(t) \sim t^{-2-\alpha}$ where α is given by the slope of the mean speed distribution $p_m(v) \sim v^{\alpha-1}$, for $v < \langle v_m \rangle$.
 464 As Pe decreases, diffusion eventually dominates over low flow speeds, thus cuts off the power-law tail of
 465 the breakthrough curves and leads to Fickian behavior from which the asymptotic dispersion coefficient
 466 D^* can be theoretically evaluated (Van Genuchten and Wierenga, 1986). However, the analysis of the
 467 displacement variance $\sigma^2(t)$ indicates that D^* cannot be measured experimentally at laboratory scale, for
 468 high values of Pe , because the distance required for reaching the asymptotic regime is orders of magnitude
 469 larger than what is workable at laboratory scale. Thus, measuring experimentally the value of α , for
 470 determining how D^* scales with Pe seems difficult.

471 The asymptotic dispersion coefficient D^* was computed up to the largest values of Pe expected for
 472 laminar flow in natural environments. Results show that $D^*/d_m \propto Pe^{2-\alpha}$ from Pe_c up to the highest
 473 value of Pe ($Pe = 4000$). Note that for the values of α expected for such heterogeneous rock samples,
 474 neither the trend $D^* \sim Pe \ln(Pe)$ (Saffman, 1959; Koch and Brady, 1985) assuming that the distribution
 475 of flow speeds is flat ($\alpha = 1$), nor the trend $D^* \sim Pe$ expected for $\alpha > 1$ at high Pe are expected. For
 476 $1 < Pe < Pe_c$, $D^*/d_m \propto Pe^{2-\alpha'}$ where $\alpha' > \alpha$ depends on the mean speed distribution and the speed
 477 decorrelation distance ℓ_c that are the parameters that determine the advective particle transition distribution
 478 and subsequently the value of Pe_c . The mean particle speed remains correlated for longer distances in
 479 porous media with straighter and larger bonds (throats). As such ℓ_c is a good indicator of the complexity
 480 of flow field, because it encompasses the effect of tortuosity that ubiquitously decreases with increasing
 481 porosity and the effect of the mean throat radius that ubiquitously increases with porosity, while the other
 482 structural parameters are distinctly different for the two sets of samples. Yet, when reported in term of
 483 number of bonds length travelled before speed decorrelates, it is observed that FS and FSD sets behave
 484 quite similarly; the equivalent number of pores (intersection nodes) crossed before losing the memory of
 485 the initial speed equals $\eta - 1$ and ranges from about 1 for $\theta = 0.1$ to about 3 for $\theta = 0.25$. We conjecture
 486 that the increase of the number nodes crossed before speed decorrelates is linked to the speed changes
 487 caused by the splitting of the flow at the network node and thus to both the mean radius of the bonds and
 488 the coordination number κ . Similar conjecture can be done for the distribution of the solute mean speed
 489 $p_m(v)$ which should be controlled by the speed changes caused by splitting of the flow where throats are
 490 connected, as it was anticipated by Alim et al. (2017) in numerical simulations in 2-dimensional simple
 491 artificial networks. The structural and hydrodynamic mechanisms that determine the flow distribution
 492 in 3-dimensional porous media, focusing on the impact pore size distribution, coordination number and
 493 local correlations on the speed distributions will be discussed in a forthcoming paper. Yet, from the results
 494 presented in this paper, one can conclude that the flow distribution, and thus the mean speed, are controlled
 495 by the distribution of fractions of fluid flowing at each of the network nodes which in turn is determined
 496 by the distribution of the throat radius (and not the mean) and the coordination number. At given porosity
 497 and mean bond radius the latter is controlled by the number of throats per unit volume that increases with
 498 porosity for the FS set and decrease with porosity for the FSD set of samples. We believe that these results
 499 give a first insight into both the mechanisms and the microstructural parameters that control dispersion in
 500 porous media.

ACKNOWLEDGMENTS

501 The authors gratefully acknowledge the support of the CNRS-PICS project CROSSCALE (Project No.
 502 280090). A. P. and M. D. gratefully acknowledge the support of the Spanish Ministry of Science and
 503 Innovation through the project HydroPore (PID2019–106887 GB-C31). Computations have been realized
 504 with the support of HPC@LR, the Center of Competence in High-Performance Computing from the
 505 Languedoc-Roussillon region, France.

REFERENCES

- 506 Alim, K., Parsa, S., Weitz, D. A., and Brenner, M. P. (2017). Local pore size correlations determine flow
 507 distributions in porous media. *Phys. Rev. Lett.* 119, 144501. doi:10.1103/PhysRevLett.119.144501
- 508 Bear, J. (1972). *Dynamics of fluids in porous media* (American Elsevier, New York)
- 509 [Dataset] Berg, C. F. (2016a). Fontainebleau 3d models. [http://www.digitalrockportal.](http://www.digitalrockportal.org/projects/57)
 510 [org/projects/57](http://www.digitalrockportal.org/projects/57). doi:doi:10.17612/P75P4P
- 511 Berg, C. F. (2016b). Fundamental transport property relations in porous media incorporating detailed pore
 512 structure description. *Transport in porous media* 112, 467–487
- 513 Bijeljic, B. and Blunt, M. J. (2006). Pore-scale modeling and continuous time random walk analysis of
 514 dispersion in porous media. *Water Resources Research* 42. doi:https://doi.org/10.1029/2005WR004578
- 515 Bijeljic, B. and Blunt, M. J. (2007). Pore-scale modeling of transverse dispersion in porous media. *Water*
 516 *Resources Research* 43. doi:https://doi.org/10.1029/2006WR005700
- 517 Bijeljic, B., Mostaghimi, P., and Blunt, M. J. (2011). Signature of non-Fickian solute transport in complex
 518 heterogeneous porous media. *Phys. Rev. Lett.* 107, 204502
- 519 Bijeljic, B., Muggerridge, A. H., and Blunt, M. J. (2004). Pore-scale modeling of longitudinal dispersion.
 520 *Water Resources Research* 40
- 521 Bijeljic, B., Raeini, A., Mostaghimi, P., and Blunt, M. J. (2013). Predictions of non-fickian solute transport
 522 in different classes of porous media using direct simulation on pore-scale images. *Physical Review E* 87.
 523 doi:10.1103/physreve.87.013011
- 524 Brenner, H. and Edwards, D. (1993). *Macrotransport Processes* (Butterworth-Heinemann, MA, USA)
- 525 Carrel, M., Morales, V. L., Dentz, M., Derlon, N., Morgenroth, E., and Holzner, M. (2018). Pore-scale
 526 hydrodynamics in a progressively bioclogged three-dimensional porous medium: 3-d particle tracking
 527 experiments and stochastic transport modeling. *Water resources research* 54, 2183–2198
- 528 Chatzis, I. and Dullien, F. A. (1985). The modeling of mercury porosimetry and the relative permeability
 529 of mercury in sandstones using percolation theory. *Int. Chem. Eng.; (United States)* 25
- 530 Danckwerts, P. (1953). Continuous flow systems: Distribution of residence times. *Chemical Engineering*
 531 *Science* 2, 1–13. doi:https://doi.org/10.1016/0009-2509(53)80001-1
- 532 De Anna, P., Le Borgne, T., Dentz, M., Tartakovsky, A. M., Bolster, D., and Davy, P. (2013). Flow
 533 intermittency, dispersion, and correlated continuous time random walks in porous media. *Physical*
 534 *review letters* 110, 184502
- 535 Delay, F., Ackerer, P., and Danquigny, C. (2005). Simulating solute transport in porous or fractured
 536 formations using random walk particle tracking. *Vadose Zone J.* 4, 360–379
- 537 Delgado, J. M. P. Q. (2006). A critical review of dispersion in packed beds. *Heat and Mass Transfer* 42,
 538 279–310
- 539 Dentz, M. (2012). Concentration statistics for transport in heterogeneous media due to stochastic
 540 fluctuations of the center of mass velocity. *Advances in Water Resources* 36, 11–22. doi:10.1016/j.
 541 [advwatres.2011.04.005](https://doi.org/10.1016/j.advwatres.2011.04.005)

- 542 Dentz, M., Borgne, T. L., Englert, A., and Bijeljic, B. (2011). Mixing, spreading and reaction in
 543 heterogeneous media: A brief review. *Journal of Contaminant Hydrology* 120-121, 1 – 17. doi:
 544 <https://doi.org/10.1016/j.jconhyd.2010.05.002>. Reactive Transport in the Subsurface: Mixing, Spreading
 545 and Reaction in Heterogeneous Media
- 546 Dentz, M., Icardi, M., and Hidalgo, J. J. (2018). Mechanisms of dispersion in a porous medium. *Journal of*
 547 *Fluid Mechanics* 841, 851–882. doi:10.1017/jfm.2018.120
- 548 Fischer, H. B. (1966). *Longitudinal dispersion in laboratory and natural streams: Report No. KH-R -12*.
 549 Tech. rep., California Inst. of Technology
- 550 Ghanbarian, B., Hunt, A. G., Ewing, R. P., and Skinner, T. E. (2014). Universal scaling of the formation
 551 factor in porous media derived by combining percolation and effective medium theories. *Geophysical*
 552 *Research Letters* 41, 3884–3890. doi:10.1002/2014GL060180
- 553 Gjetvaj, F., Russian, A., Gouze, P., and Dentz, M. (2015). Dual control of flow field heterogeneity
 554 and immobile porosity on non-fickian transport in berea sandstone. *Water Resources Research* 51,
 555 8273–8293. doi:10.1002/2015WR017645
- 556 Gouze, P., Borgne, T. L., Leprovost, R., Lods, G., Poidras, T., and Pezard, P. (2008). Non-fickian dispersion
 557 in porous media: 1. Multiscale measurements using single-well injection withdrawal tracer tests. *Water*
 558 *Resources Research* 44. Doi:10.1029/2007WR006278
- 559 Gouze, P., Puyguiraud, A., Roubinet, D., and Dentz, M. (2021). Pore-scale transport in rocks of different
 560 complexity modeled by random walk methods. *Transport in Porous Media* , 1573–1634doi:10.1007/
 561 s11242-021-01675-2
- 562 Guibert, R., Horgue, P., Debenest, G., and Quintard, M. (2016). A comparison of various methods for the
 563 numerical evaluation of porous media permeability tensors from pore-scale geometry. *Mathematical*
 564 *Geosciences* 48, 329–347
- 565 Han, N.-W., Bhakta, J., and Carbonell, R. G. (1985). Longitudinal and lateral dispersion in packed
 566 beds: Effect of column length and particle size distribution. *AIChE Journal* 31, 277–288. doi:<https://doi.org/10.1002/aic.690310215>
- 567 [//doi.org/10.1002/aic.690310215](https://doi.org/10.1002/aic.690310215)
- 568 Icardi, M., Boccardo, G., Marchisio, D. L., Tosco, T., and Sethi, R. (2014). Pore-scale simulation of fluid
 569 flow and solute dispersion in three-dimensional porous media. *Physical Review E* 90, 013032
- 570 Kang, P. K., de Anna, P., Nunes, J. P., Bijeljic, B., Blunt, M. J., and Juanes, R. (2014). Pore-scale
 571 intermittent velocity structure underpinning anomalous transport through 3-d porous media. *Geophysical*
 572 *Research Letters* 41, 6184–6190. doi:10.1002/2014GL061475
- 573 Kinzel, D. L. and Hill, G. A. (1989). Experimental study of dispersion in a consolidated sandstone. *The*
 574 *Canadian Journal of Chemical Engineering* 67, 39–44. doi:<https://doi.org/10.1002/cjce.5450670107>
- 575 Koch, D. L. and Brady, J. F. (1985). Dispersion in fixed beds. *Journal of Fluid Mechanics* 154, 399–427.
 576 doi:10.1017/s0022112085001598
- 577 Koponen, A., Kataja, M., and Timonen, J. (1996). Tortuous flow in porous media. *Physical Review E* 54,
 578 406
- 579 Lee, T., Kashyap, R., and Chu, C. (1994). Building skeleton models via 3-d medial surface axis thinning
 580 algorithms. *CVGIP: Graphical Models and Image Processing* 56, 462–478. doi:[https://doi.org/10.1006/](https://doi.org/10.1006/cgip.1994.1042)
 581 [cgip.1994.1042](https://doi.org/10.1006/cgip.1994.1042)
- 582 Levy, M. and Berkowitz, B. (2003). Measurement and analysis of non-Fickian dispersion in heterogeneous
 583 porous media. *Journal of contaminant hydrology* 64, 203–226
- 584 Li, M., Qi, T., Bernabé, Y., Zhao, J., Wang, Y., Wang, D., et al. (2018). Simulation of solute transport
 585 through heterogeneous networks: analysis using the method of moments and the statistics of local
 586 transport characteristics. *Scientific Reports* 8. doi:10.1038/s41598-018-22224-w

- 587 Matyka, M., Golembiewski, J., and Koza, Z. (2016). Power-exponential velocity distributions in disordered
588 porous media. *Phys. Rev. E* 93, 013110. doi:10.1103/PhysRevE.93.013110
- 589 Morales, V. L., Dentz, M., Willmann, M., and Holzner, M. (2017). Stochastic dynamics of intermittent
590 pore-scale particle motion in three-dimensional porous media: Experiments and theory. *Geophysical*
591 *Research Letters* 44, 9361–9371
- 592 Moroni, M. and Cushman, J. H. (2001). Statistical mechanics with three-dimensional particle tracking
593 velocimetry experiments in the study of anomalous dispersion. II. experiments. *Physics of Fluids* 13,
594 81–91. doi:10.1063/1.1328076
- 595 Oren, P.-E. (2002). Process based reconstruction of sandstones and prediction of transport properties.
596 *Transport in porous media* 46, 311–343
- 597 Pfannkuch, H. O. (1963). Contribution a l'étude des déplacements de fluides miscibles dans un milieu
598 poreux. *Rev. Inst. Fr. Petr.* 18, 215–270
- 599 Puyguiraud, A., Gouze, P., and Dentz, M. (2019a). Is there a representative elementary volume for
600 anomalous dispersion? *Transport in Porous Media* doi:10.1007/s11242-019-01366-z
- 601 Puyguiraud, A., Gouze, P., and Dentz, M. (2019b). Stochastic dynamics of lagrangian pore-scale velocities
602 in three-dimensional porous media. *Water Resources Research* 55. doi:10.1029/2018WR023702
- 603 Puyguiraud, A., Gouze, P., and Dentz, M. (2019c). Upscaling of anomalous pore-scale dispersion.
604 *Transport in Porous Media*
- 605 Puyguiraud, A., Gouze, P., and Dentz, M. (2021). Pore-scale mixing and the evolution of hydrodynamic
606 dispersion in porous media. *Phys. Rev. Lett.* 126, 164501. doi:10.1103/PhysRevLett.126.164501
- 607 Russian, A., Dentz, M., and Gouze, P. (2016). Time domain random walks for hydrodynamic transport in
608 heterogeneous media. *Water Resources Research* 52, 3309–3323. doi:10.1002/2015WR018511
- 609 Saffman, P. G. (1959). A theory of dispersion in a porous medium. *Journal of Fluid Mechanics* 6, 321–349
- 610 Sahimi, M. (2011). *Flow and transport in porous media and fractured rock: from classical methods to*
611 *modern approaches* (John Wiley & Sons)
- 612 Sahimi, M., Hughes, B. D., Scriven, L., and Davis, H. T. (1986). Dispersion in flow through porous
613 media—i. one-phase flow. *Chemical engineering science* 41, 2103–2122
- 614 Sahimi, M. and Imdakm, A. (1988). The effect of morphological disorder on hydrodynamic dispersion in
615 flow through porous media. *Journal of Physics A* 21, 3833–3870
- 616 Seymour, J. D. and Callaghan, P. T. (1997). Generalized approach to nmr analysis of flow and dispersion
617 in porous media. *AIChE Journal* 43, 2096–2111. doi:https://doi.org/10.1002/aic.690430817
- 618 Seymour, J. D., Gage, J. P., Codd, S. L., and Gerlach, R. (2004). Anomalous fluid transport in porous
619 media induced by biofilm growth. *Physical Review Letters* 93. doi:10.1103/physrevlett.93.198103
- 620 Siddiqi, K. and Pizer, S. (2008). *Medial Representations: Mathematics, Algorithms and Applications*
621 (Springer Publishing Company, Incorporated), 1st edn.
- 622 Siena, M., Riva, M., Hyman, J. D., Winter, C. L., and Guadagnini, A. (2014). Relationship between pore
623 size and velocity probability distributions in stochastically generated porous media. *Phys. Rev. E* 89,
624 013018. doi:10.1103/PhysRevE.89.013018
- 625 Souzy, M., Lhuissier, H., Méheust, Y., Borgne, T. L., and Metzger, B. (2020). Velocity distributions,
626 dispersion and stretching in three-dimensional porous media. *Journal of Fluid Mechanics* 891. doi:10.
627 1017/jfm.2020.113
- 628 Taylor, G. (1953). Dispersion of soluble matter in solvent flowing slowly through a tube. In *Proceedings of*
629 *the Royal Society of London A: Mathematical, Physical and Engineering Sciences* (The Royal Society),
630 vol. 219, 186–203

- 631 Van Genuchten, M. T. and Wierenga, P. J. (1986). *Solute Dispersion Coefficients and Retardation Factors*
632 (John Wiley Sons, Ltd), chap. 44. 1025–1054. doi:<https://doi.org/10.2136/sssabookser5.1.2ed.c44>
- 633 Weller, H. G., Tabor, G., Jasak, H., and Fureby, C. (1998). A tensorial approach to computational continuum
634 mechanics using object-oriented techniques. *Computers in physics* 12, 620–631
- 635 Whitaker, S. (1967). Diffusion and dispersion in porous media. *AIChE Journal* 13, 420–427. doi:<https://doi.org/10.1002/aic.690130308>
636

FIGURE CAPTIONS

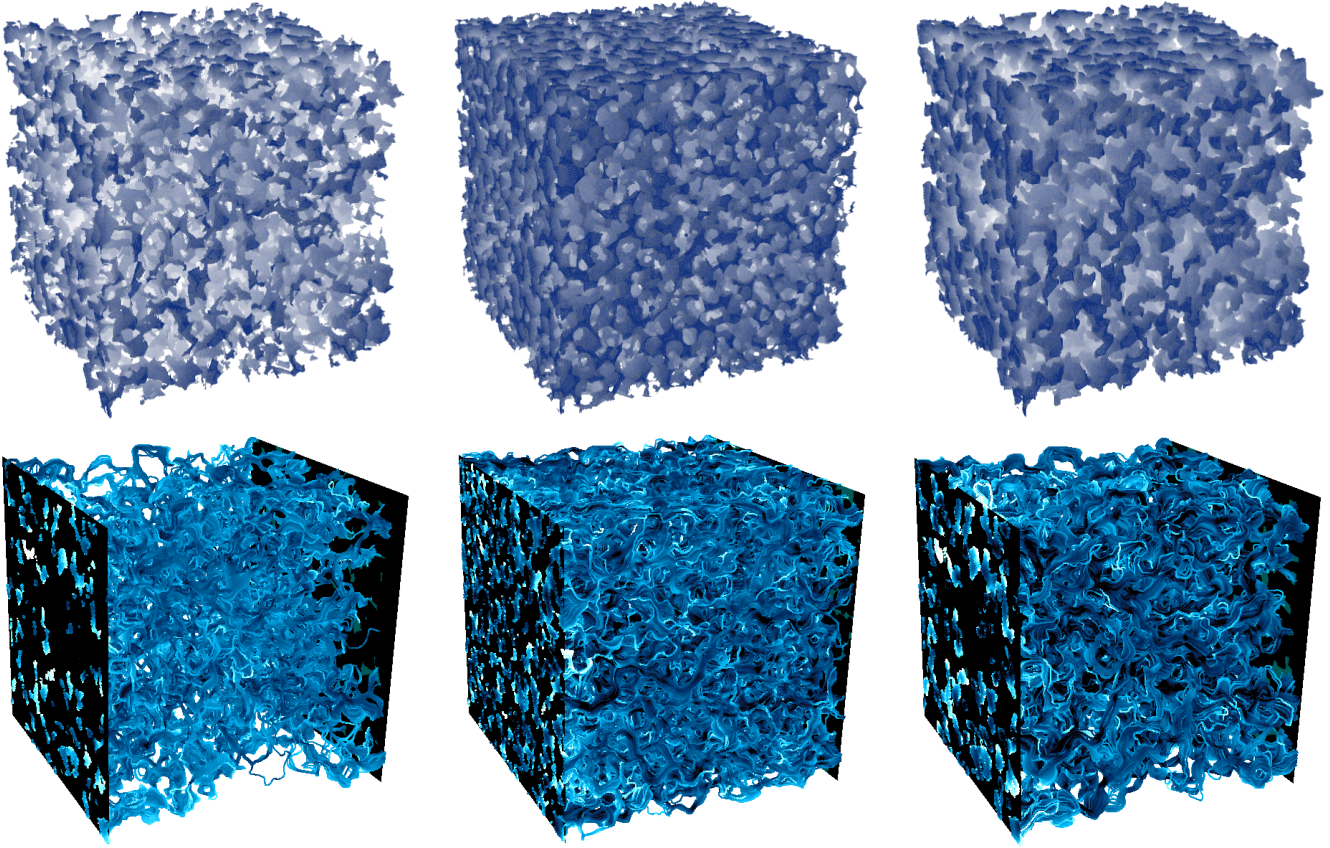


Figure 1. Three-dimensional structure of *FS10* (left), *FS25* (middle), *FSD25* (right) samples. The top row displays the void space. The lines in the bottom panel show particle paths, the color scheme indicating the particle speed from white ($u/\langle u \rangle \leq 7 \times 10^{-4}$) to dark blue ($u/\langle u \rangle = 10$).

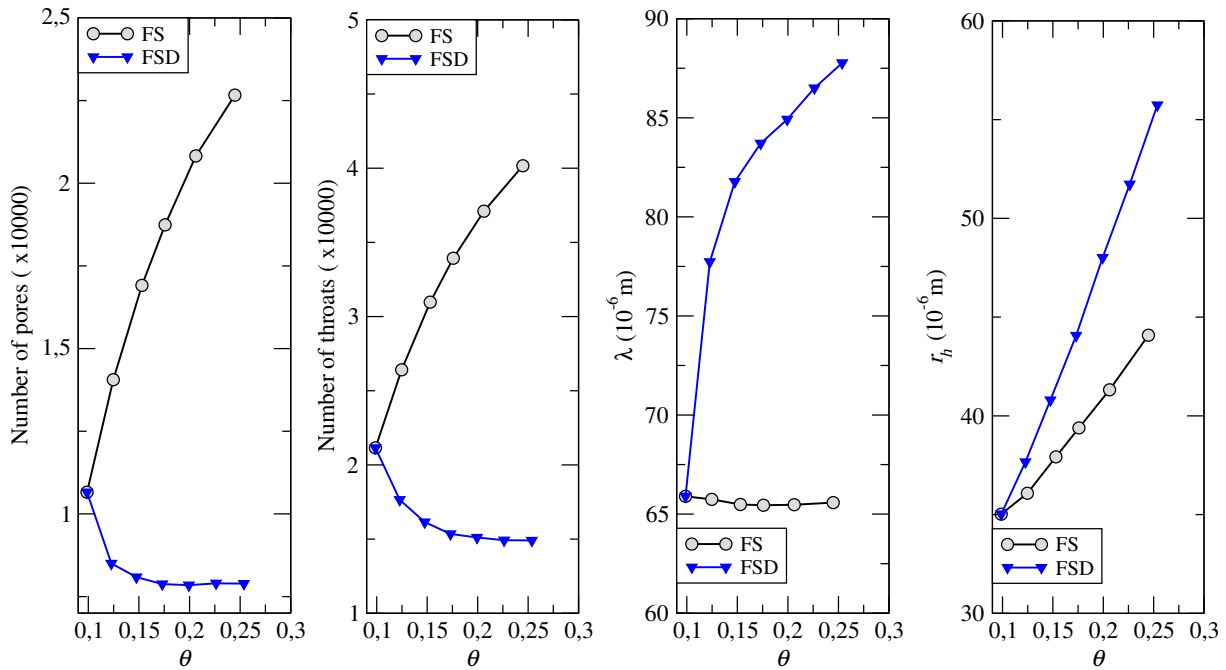


Figure 2. From left to right panels: number of pores; number of throats; mean throat length λ ; mean throat radius r_h versus porosity θ for the *FS* and *FSD* samples.

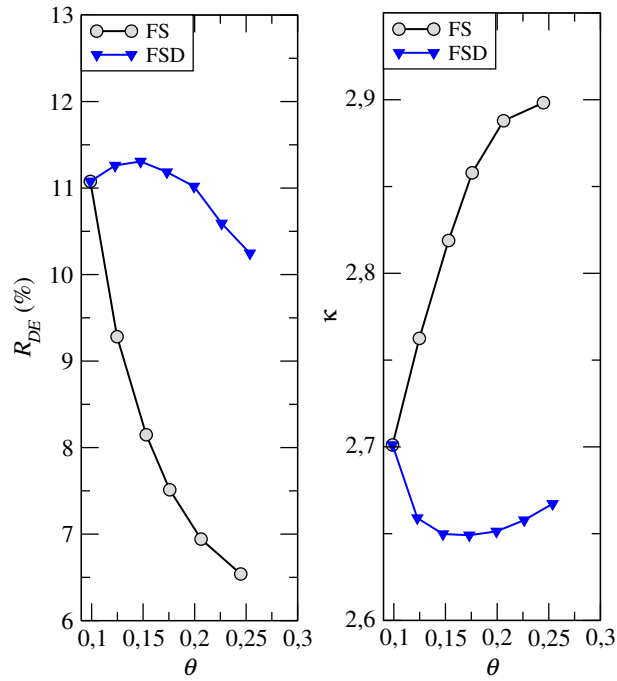


Figure 3. Left, ratio (in %) of the number of dead-ends to the number of throats; right, mean number of throats per pore κ versus porosity θ for the *FS* and *FSD* samples.

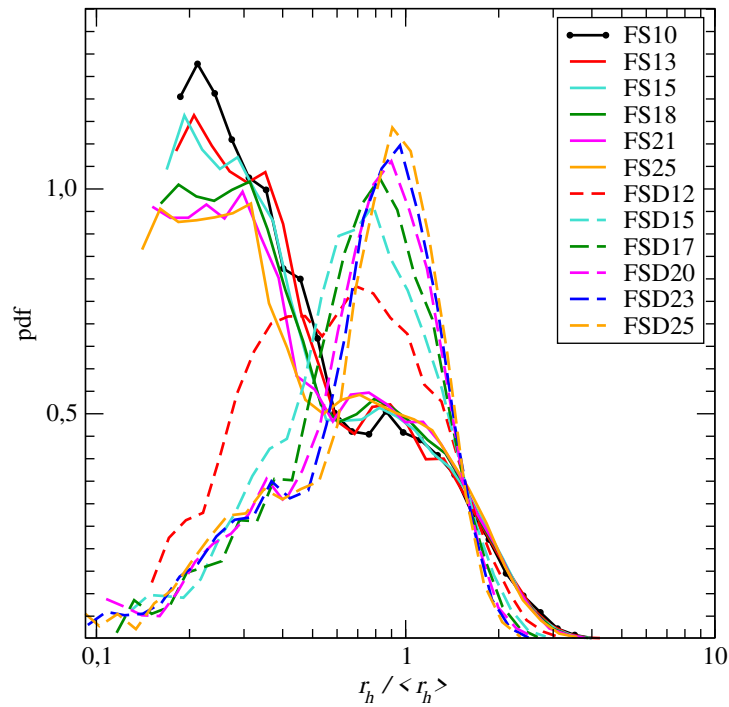


Figure 4. Normalized distribution of r_h for the *FS* and *FSD* samples.

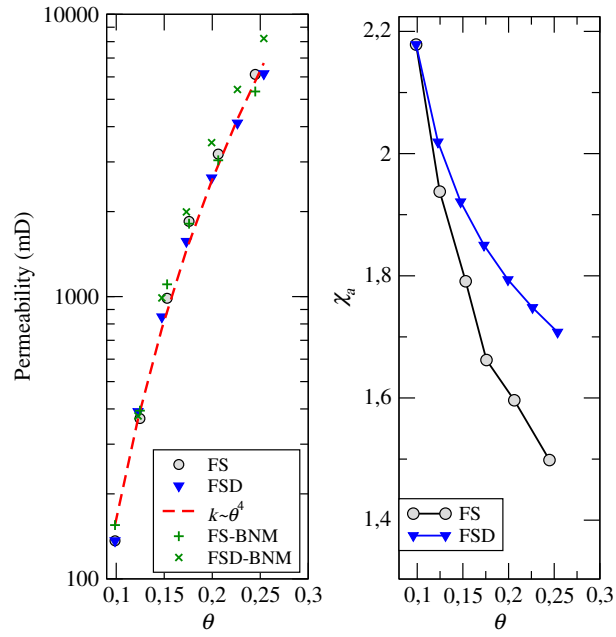


Figure 5. Permeability (left panel) and advective tortuosity χ_a (right panel) versus porosity θ for the *FS* and *FSD* samples.

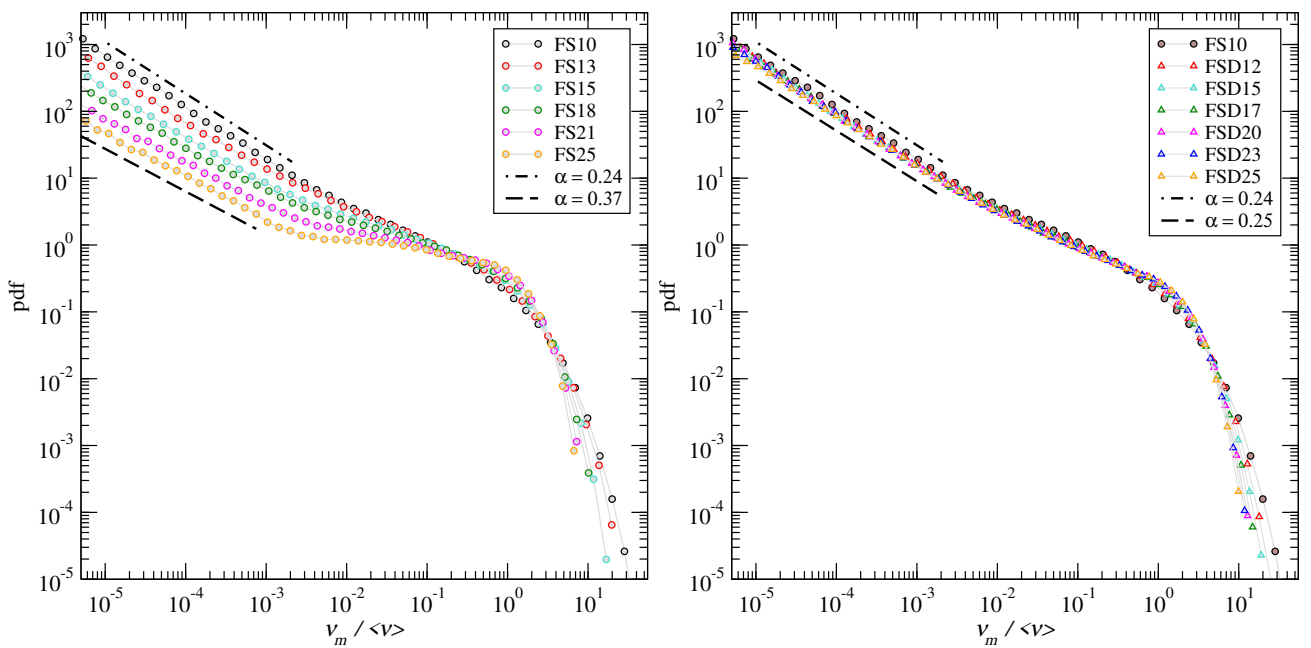


Figure 6. Distribution of the Eulerian mean speeds $p_m(v)$ normalized to its mean, for the *FS* (left panel) and the *FSD* (right panel) samples.

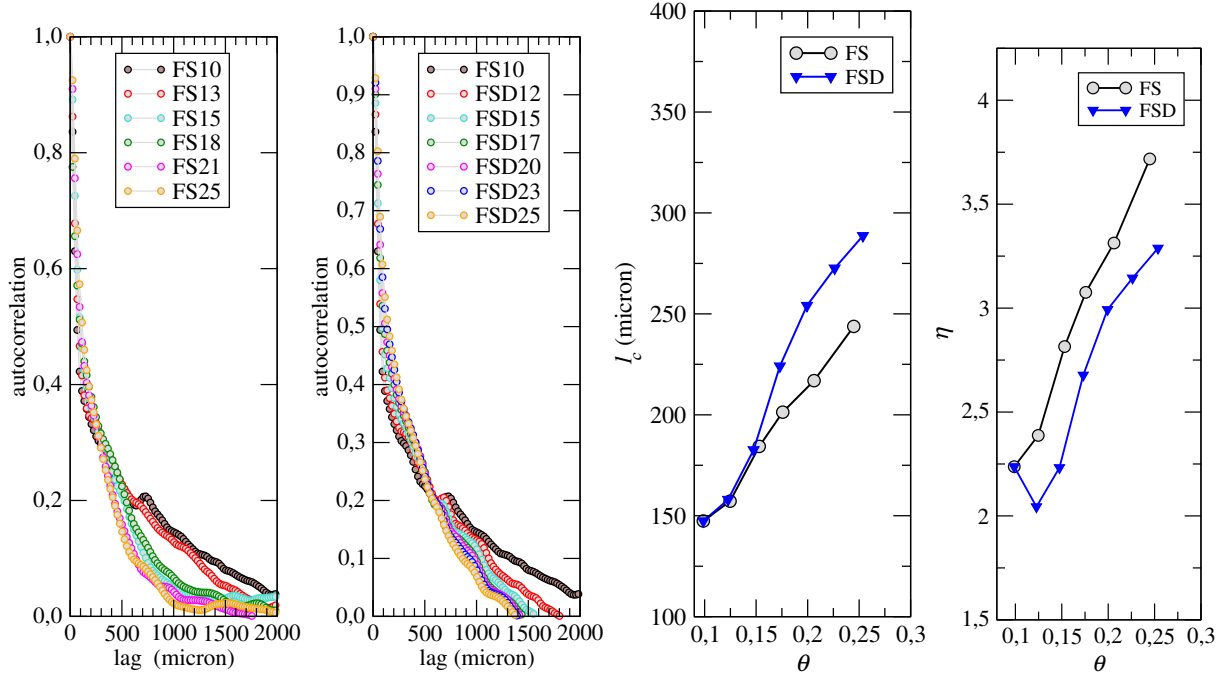


Figure 7. Flux weighted Langrangian speed auto-correlation function $\Upsilon_{v_v}(l)$ for the *FS* (left panel) and the *FSD* (middle-left panel) samples. The middle-right panel displays the decorrelation length ℓ_c and the right panel displays the ratio $\eta = \ell_c/\lambda$ versus porosity.

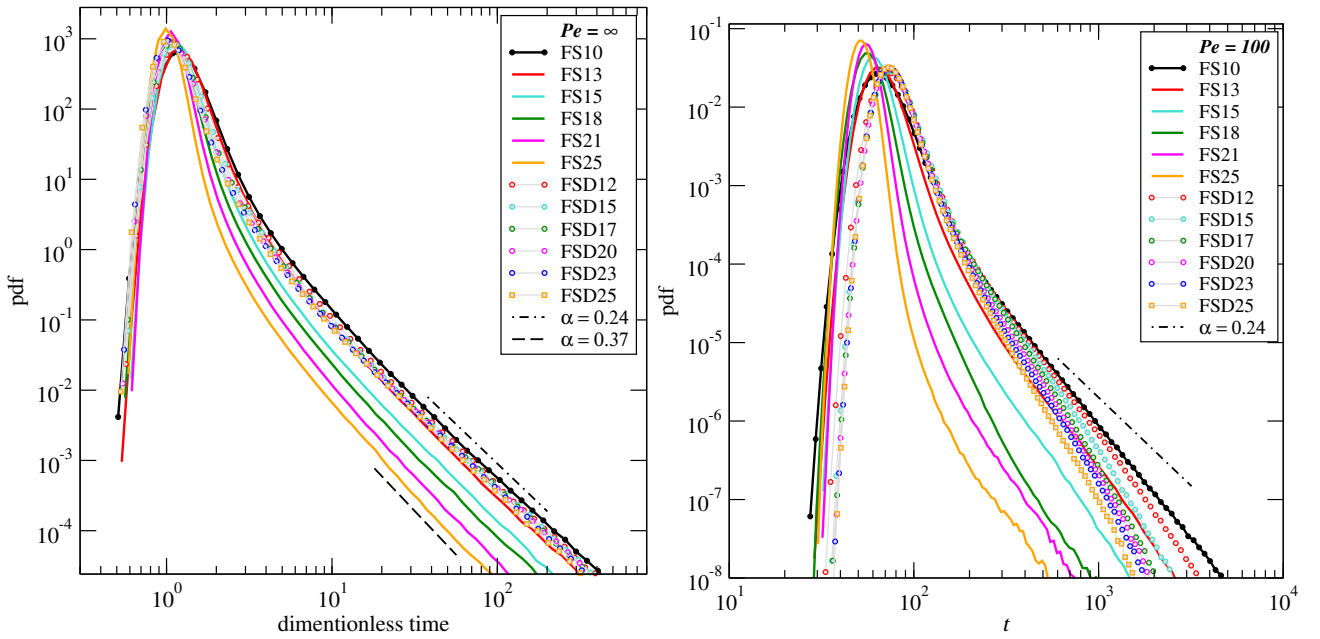


Figure 8. First passage time PDF f_t at $Z = 5.47 \times 10^{-2}$ m from the inlet. Left: results for infinite Pe versus dimensionless time Z/v . Right: results for $Pe = 100$ versus time.

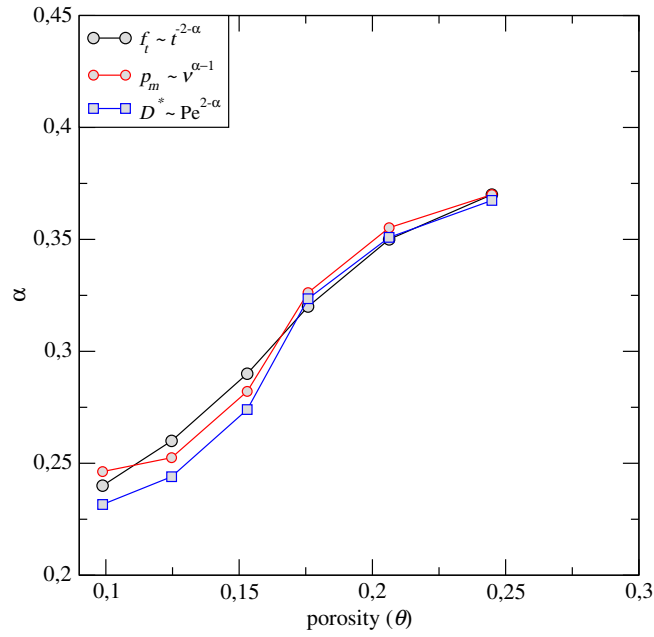


Figure 9. Comparison of the value of α for the FS samples evaluated from 1) the slope of the first passage time plotted in the left panel, 2) the slope of the mean speed PDF plotted in Figure 6 and 3) the slope of the D^*/d_m versus Pe plotted in Figure 11.

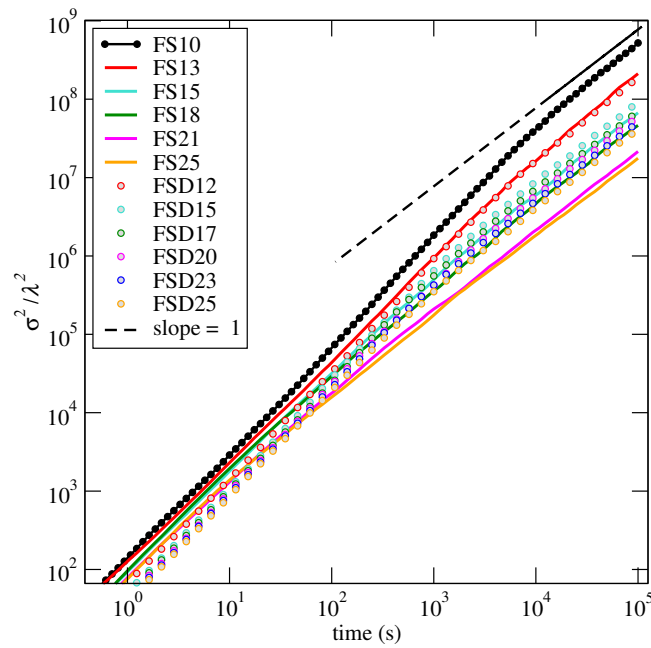


Figure 10. Normalized z -direction displacement variance versus time for $Pe = 100$.

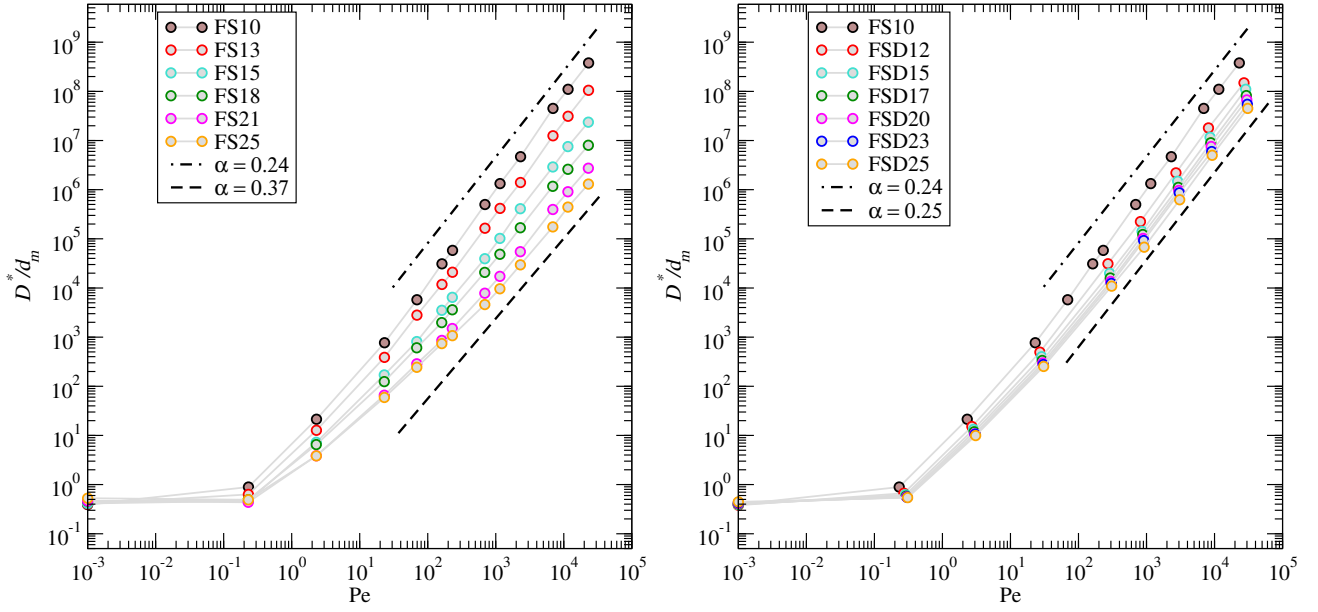


Figure 11. Asymptotic dispersion coefficient versus Pe for the FS and FSD samples

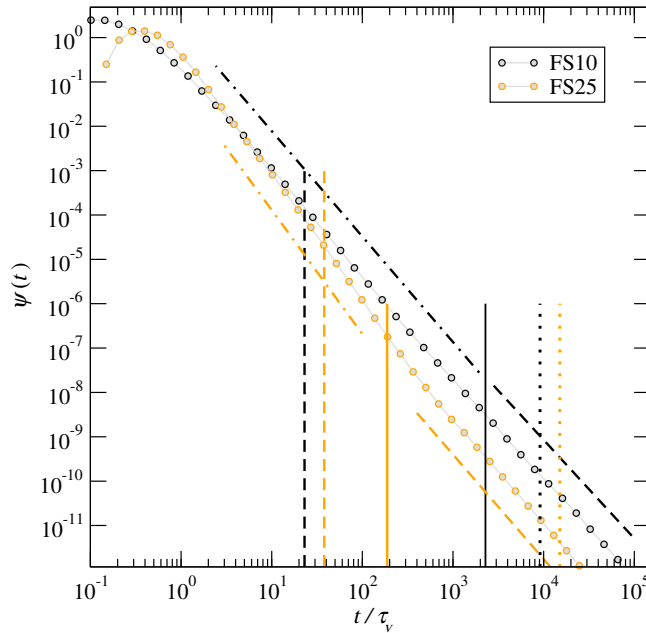


Figure 12. Distribution of advective transition times rescaled by τ_v for $FS10$ and $FS25$. The dimensionless cut-off time is $Pe = \tau_D/\tau_v$. The vertical lines denote $Pe = 10$ (dashed lines), $Pe = Pe_c$ (solid lines) and $Pe = 4000$ (dot line). The sloped lines denote the power-law behaviors $t^{-2-\alpha'}$ for $Pe < Pe_c$ with $\alpha' = 0.38$ and 0.79 for $FS10$ and $FS25$, respectively and $t^{-2-\alpha}$ for $Pe \geq Pe_c$ with $\alpha = 0.23$ and 0.37 for $FS10$ and $FS25$, respectively.